Scalable Synthesis of Acidic Mesostructured Silica–Carbon Nanocomposite Catalysts by Rotary Evaporation

Ruyi Zhong,[a] Li Peng,*[b] Remus Ion Iacobescu,[c] Yiannis Pontikes,[c] Riyang Shu,[d] Longlong Ma,[d] and Bert F. Sels*[a]

A practical and scalable synthesis for the mass production of well-ordered mesoporous silica–carbon composites by using a fast rotary-evaporation-induced self-assembly method in the absence of any additional support is presented.

Well-ordered mesoporous materials with large pore sizes have attracted great attention because of facilitated transport of molecules within the porous structure, which has promising applications in areas such as catalysis, adsorption, gas separation, and drug delivery.[1–5] Considerable efforts have been undertaken to incorporate organic components within an inorganic silica framework to form silica–carbon nanocomposites to achieve symbiosis of the properties of both components.[1,3] These porous silica–carbon structures can be synthesized by using direct soft-template approaches, which avoids the extra step of creating templating silica structures by aqueous[6] or evaporation-induced self-assembly (EISA)[3,7–9] routes. The EISA process is a rapid and well-established approach to synthesize well-defined mesostructured nanocomposite materials.[3,9,10] Typical EISA syntheses take place in the form of thin films (TF-EISA), and nanocomposite self-assembly is driven by evaporation during film deposition.[10,11] Despite its beauty for thin-film applications, success in producing mass quantities of mesostructured composite powders, for example, by using EISA with thicker films, is scarce.[12,13] Given that the TF-EISA process
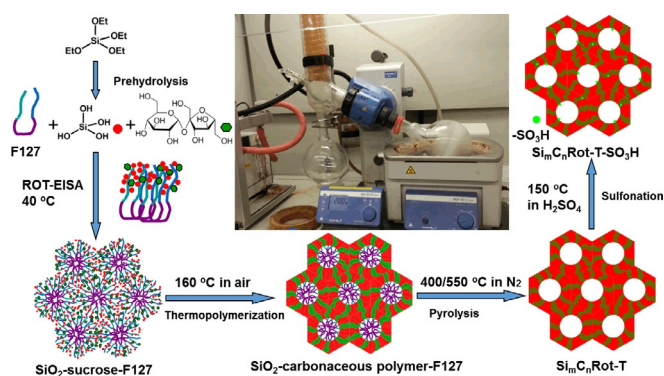
[a] R. Zhong, Prof. Dr. B. F. Sels
Centre for Surface Science and Catalysis
KU Leuven, Corelab
Celestijnenlaan 200
B3001 Heverlee (Belgium)
E-mail: bert.sels@biw.kuleuven.be

[b] Dr. L. Peng
State Key Laboratory of Materials-Oriented Chemical Engineering,
College of Chemistry and Chemical Engineering
Nanjing Tech University
5 Xinmofan Road
Nanjing 210009 (P. R. China)
E-mail: lisa.lipeng@gmail.com

[c] Dr. R. I. Iacobescu, Prof. Dr. Y. Pontikes
Department of Materials Engineering
KU Leuven
Kasteelpark Arenberg 44
3001 Heverlee (Belgium)

[d] R. Shu, Prof. Dr. L. Ma
Key Laboratory of Renewable Energy
Guangzhou Institute of Energy Conversion, Chinese Academy of Sciences
Guangzhou 510640 (P. R. China)

utilizes a concentration gradient to induce the ordering of precursors around templates starting from liquid–vapor interfaces,[2,4,10,14] poorer organization is expected with increased thickness of the liquid film;[11,15–17] mass transport of the solvent will be hindered, the sol–gel reaction time of the precursors will increase, multiple phases are expected, and so on. Except for the thickness of the film, the evaporation rate[12] as well as the relative humidity[11] are essential parameters that control the meso-organization. Whereas TF-EISA, which can be performed by petri-dish coating,[7,9] dip coating,[11,14,18] and spin coating,[19] is a clear choice for mesoporous thin films with excellent substrate adhesion, it is not preferred to synthesize porous composite powders. A vessel with a large surface is required to realize interfacial assembly of the mesostructures during fast evaporation, whereas sample collection (by scraping) is very laborious, if not unrealistic, for large-scale production.

To cope with these issues, Lu and co-workers presented a first adaption of the classic EISA method by developing an EISA-based aerosol process.[8] Though the aerosol composites were practical in conduction applications, it would be difficult to implement the aerosol apparatus in the laboratory and at the industrial scale. Another elegant alternative was presented by Zhao and co-workers. They used polyurethane foam as a decomposable macroporous 3D scaffold for evaporation-induced coating of a mesoporous resin–silica composite. Remaining challenges include the presence of residual carbon from the sacrificial skeleton in the final composite and a long solvent evaporation time (5 to 8 h).[20] To sufficiently control and enhance the drying rate during evaporation and to realize mass production of mesoporous silica–carbon nanocomposite powders, we herein communicate a novel facile rotary evaporation synthesis method (denoted ROT-EISA).

The setup of this new method used standard rotary evaporation equipment (Scheme 1). Interestingly, the application of vacuum not only allowed control of the evaporation rate over free evaporation in air, but foaming under the reduced pressure created additional macroporosity, which allowed "thin-film"-like processes to occur without the classic plate support. Moreover, the rotation movement ensured macroscopic uniformity. The starting triconstituent precursor solution responsible for the formation of the mesopore structure was similar to that used in classic EISA, and it consisted of tetraethyl orthosilicate (TEOS) and sucrose (representing the silica and carbon precursors, respectively), in addition to F127, which was the structure-directing agent.[7,21] Whereas the volatiles in the ROT-EISA process were rapidly removed under reduced pressure

Scheme 1. Synthesis scheme for the preparation of silica–carbon nanocomposites by rotary evaporation.

Figure 1. TEM images of a) $Si_{66}C_{33}$Rot-400 and b) $Si_{66}C_{33}$Rot-400-SO_3H. c) N_2 sorption isotherms and d) XRD patterns of $Si_{66}C_{33}$Rot-400 (black) and $Si_{66}C_{33}$TF-400-SO_3H (red).

and rotation, a crushable solid of the well-ordered mesoporous silica–carbon nanocomposite structure, similar to that of the conventional TF-EISA materials, was formed. Its trimodal micro/meso/macroporosity, as ascertained by structural analysis and explained below, may be beneficial for molecular transport through the composite material, and therefore, catalysis was selected to prove the composite's usefulness. After decoration with sulfonic acid groups, the porous composite was capable of catalyzing the ethanolysis of fructose to 5-(hydroxymethyl)-furfural (HMF) ethers and the condensation of sylvan with furfural, two relevant biomass-related test reactions.

In a typical synthesis, F127 (6.4 g) was dissolved in a solution containing ethanol (32.0 g) and HCl (37 wt%, 0.3 g) under magnetic stirring in a 40 °C H_2O bath. Then, sucrose (2.8 g) in H_2O (10 g) was mixed with TEOS (8.32 g, for the initial silica carbon ratio for $Si_{66}C_{33}$) and added to the template F127 solution. The mixture was continuously stirred in the 40 °C water bath for another 1 h. After that, the precursor solution was transferred into a 1 L round-bottomed flask, which was connected to a rotary evaporator, half immersed in a water bath of 40 °C. After starting rotation at 200 rpm, the pressure was decreased under evacuation, which induced fast solvent removal and foaming. In 10 min, the pressure decreased to approximately 10.0 kPa, the internal wall of the flask was covered with the silica–sucrose–F127 gel, and no more substantial droplets were observed at the condenser pipe of the rotary evaporator. Rotation and evacuation were continued for another 1 h. The total solvent evaporation and self-assembly time is drastically shortened relative to that of the TF-EISA process (usually ≈ 20 h).[7,21] The as-formed foamed gel was then cured at 160 °C for 24 h in air, which was followed by pyrolysis at 400 (or 550 °C) to give the composite $Si_{66}C_{33}$Rot-400 (or $Si_{66}C_{33}$Rot-550). The SO_3H groups were successfully introduced to produce $Si_{66}C_{33}$Rot-400-SO_3H and $Si_{66}C_{33}$Rot-550-SO_3H by sulfonation in a closed autoclave by using concentrated H_2SO_4 at 150 °C for 15 h;[7,22] this afforded SO_3H site densities of 0.31 and 0.23 mmol g^{-1}, respectively. Sulfonation of the silica–carbon nanocomposite had no influence on the structural properties owing to the presence of the rigid silicate structure in the composite (Figure 1 a, b), as previously reported.[7]
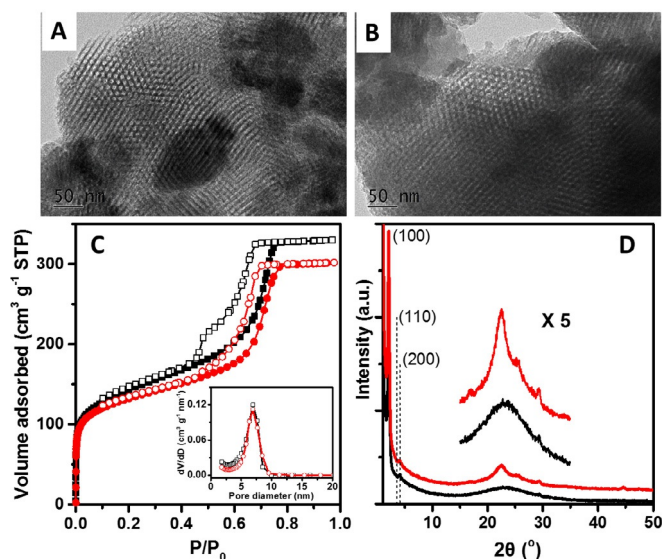
The macroscopic appearance of the as-synthesized gel after curing at 160 °C was very different from that of the standard TF-EISA in dishes. The fast drying and rotation caused a foaming gel that cracked and peeled off the glass wall. In contrast, the thin film in the classic TF-EISA usually strongly sticks to the glass substrate, which turns into flakes only after intense scraping. The microscopic morphologies, shown by the SEM images of $Si_{66}C_{33}$Rot-400-SO_3H and $Si_{66}C_{33}$TF-400-SO_3H (Figure S1 in the Supporting Information) are notably different. The voids formed by rotary evaporation of the solvents were bigger and irregular (≈ 5 μm), whereas evaporation of the thin film usually led to evenly distributed small holes (≈ 1 μm). The foam-like structure and visible cracks in the rotary material were a result of fast solvent removal under vacuum. Despite the irregular macroscopic pore structure, high-resolution electron probe microanalysis (HR EPMA) mapping (Figure 2) revealed a homogeneous distribution of the C, Si, S, and O elements for $Si_{66}C_{33}$Rot-400-SO_3H, as in case of the standard $Si_{66}C_{33}$TF-400-SO_3H, which evidenced the formation of a genuine composite
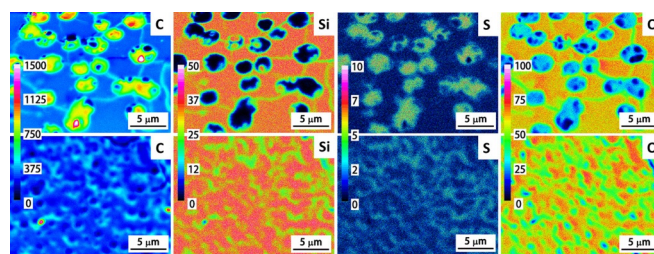
Figure 2. Elemental distribution maps of C, Si, S, and O in $Si_{66}C_{33}$Rot-400-SO_3H (top) and $Si_{66}C_{33}$TF-400-SO_3H (bottom). The colored scale bars show the level of elemental concentration. EPMA mapping conditions: 7 kV, 15 nA, 33 nm step size (in x and y) and a counting time of 40 ms per step. Each map is 30 μm × 22.5 μm. The sample was embedded in resin, which was polished and coated with a Pt–Pd layer after hardening.

with entangling silica and carbon phases, despite the nonequilibrium process during evaporation.

$Si_{66}C_{33}Rot-400$ was found to possess a well-ordered hexagonal mesoporous structure, as judged from the typical H_1-type hysteresis loop in the N_2 physisorption isotherm (at $-196\,°C$) (Figure 1 c), the diffraction patterns in the low-angle region (Figure 1 d), and its TEM image (Figure 1 a). This image shows highly uniform cylindrical pores approximately 7 nm in size in 2D hexagonal structures, very close to the structure of $Si_{66}C_{33}TF-400$, though its desorption branch to the lower limit of the hysteresis in the isotherm may fall more steeply, which is indicative of the presence of some disordered domains from slight collapse of the cylindrical pore structure. The slight loss in structural ordering may result from conformational changes in the F127 copolymer induced by rotation. The material also exhibits micropores coming from voids in the organic phase, as previously explained.[7] In contrast to classic TF-EISA, synthesis by the ROT-EISA method is highly reproducible, as derived from the thermogravimetric analysis (TGA) curves and the N_2 sorption isotherms of the samples from three parallel batches (Figure S2).

The mechanism for the formation of the mesostructure during ROT-EISA is proposed in Scheme 1, in analogy to that during TF-EISA.[7] They are both solvent-evaporation driven processes, in which volatiles such as ethanol, water, and HCl are rapidly removed; this forces the nonvolatiles such as sucrose, silica oligomers, and F127 to cohabit within a confined volume. Their progressively increasing concentrations drive self-assembly of silica–sucrose–F127 micelles and their further organization into lyotropic liquid crystalline mesophases. Silica oligomers and sucrose stay in the poly(ethyleneoxide) (PEO) domains of F127, which surround the poly(propylene oxide) (PPO) domains owing to H-bonding of the OH groups of silica and sucrose with the hydrophilic F127 PEO blocks. Besides, under the mild acidic conditions (0.05 M HCl), the PEO blocks and the OH groups of the precursor are partially protonated, and their Coulombic interaction with the chloride anions acts as a simultaneous driving force for structural assembly.[4] The curing and pyrolysis procedure leads to an interpenetrating network between the mesoporous silica and the nanosized carbon phases as a result of nanoscaled phase separation. Entanglement of the silica and carbon phases is evidenced by the remaining ordered mesostructured silica after carbon removal (by calcination in air) of the parent composite. The volume of the mesopores (V_{meso}) increases (from 0.40 to 0.50 $cm^3 g^{-1}$) and the volume of the micropores (V_{micro}) decreases (from 0.10 to 0.03 $cm^3 g^{-1}$), whereas the structured mesopores are still of the same diameter (6.9 nm). Removal of the nanosized carbon phases in the composite pore walls creates new voids, which contribute to V_{meso} in the formed silica-only material, whereas the micropores are mostly eliminated, as they are mainly associated with the carbon phase.[7]

The total carbon contents of both the TF- and ROT-EISA samples, pyrolyzed at two different temperatures, were analyzed by TGA (Figure S3). Elevating the pyrolysis temperature from 400 to 550 °C decreased the carbon content owing to the higher degree of carbonization, that is, the growth of polycyclic aromatic carbon sheets and the removal of surface oxygen-containing groups. The decrease went from 29 to 27 wt% for the $Si_{66}C_{33}Rot-T-SO_3H$ samples and from 31 to 23 wt% for the $Si_{66}C_{33}TF-T-SO_3H$ samples. The relative variation in C=O to C=C could be observed in the FTIR spectra (Figure S4). Inspection of the differential thermogravimetry (DTG) curves in Figure S3 reveals a higher percentage of carbon species in the high-temperature range for the TF-EISA samples. These samples (e.g., $Si_{66}C_{33}TF-400-SO_3H$) show additional weak reflections (with $2\theta = 15–35°$) assigned to the presence of graphite-like carbon (Figure 1 d),[22] whereas the ROT-EISA samples (e.g., $Si_{66}C_{33}Rot-400$) only show a broad peak due to amorphous carbon. The S 2p X-ray photoelectron spectra of $Si_{66}C_{33}Rot-400-SO_3H$ and $Si_{66}C_{33}TF-400-SO_3H$ in Figure S5 show single peaks at a binding energy of approximately 169 eV for both, which indicates that S is mainly present in the form of sulfonate groups. The calculated surface concentration of SO_3H is similar for both materials, whereas the peak position for $Si_{66}C_{33}Rot-400-SO_3H$ is shifted to a lower binding energy by 0.4 eV. These results indicate that the carbon phases in the ROT-EISA samples are less prone to carbonization than those in the TF-EISA composites, that is, polyfuranics are present in higher contents than polyaromatics. This is probably due to faster removal of HCl under rotary evaporation, which catalyzes the formation and cross-linking of furanic intermediates from sucrose in the initial synthesis stage.

The sulfonated silica–carbon nanocomposites were evaluated in catalytic reactions for the ethanolysis of fructose[23–25] and the condensation of 2-methylfuran (sylvan) with furfural.[26–29] The reaction results in the presence of $Si_{66}C_{33}Rot-400-SO_3H$ and $Si_{66}C_{33}Rot-550-SO_3H$ were compared with those of the standards $Si_{66}C_{33}TF-400-SO_3H$ and $Si_{66}C_{33}TF-550-SO_3H$, respectively. The results are shown in Figure 3. Fructose conversion was equally fast for both materials and comparable products were formed. For the ethanolysis of fructose to 5-ethoxymethylfurfural (EMF) and ethyl levulinate (EL), both of which are candidates for next-generation biofuels, a detailed reaction mechanism was reported in previous work.[23–25] The same model was used to fit the different kinetic profiles. As the $Si_{66}C_{33}Rot-T-SO_3H$ and $Si_{66}C_{33}TF-T-SO_3H$ catalysts showed similar kinetic (product distribution) profiles (see Figure 3 a, b), similar ethanolysis mechanisms and kinetics govern the reaction in the presence of both nanocomposites. The main reaction pathways include the dehydration of fructose to HMF, the etherification of HMF to EMF or its direct ethanolysis to EL, and the rehydration of EMF to EL. The side reactions include the interconversion of fructose and difructose anhydride, the interconversion of fructose and glucosides, and the degradation of fructose and HMF into humins. The micropore volumes, suggested earlier to dominate the fructose ethanolysis reaction, of $Si_{66}C_{33}Rot-T-SO_3H$ are very close to those of $Si_{66}C_{33}TF-T-SO_3H$ (Table S1), which may lead them to exhibit similarly high catalytic activities for the ethanolysis of fructose.

For the condensation of sylvan with furfural, hydroxyalkylation of a furan ring with aldehyde to form an alcohol, and subsequent alkylation of the alcohol with another furan give rise to the targeted product, 2,2′-(2-furylmethylene)bis
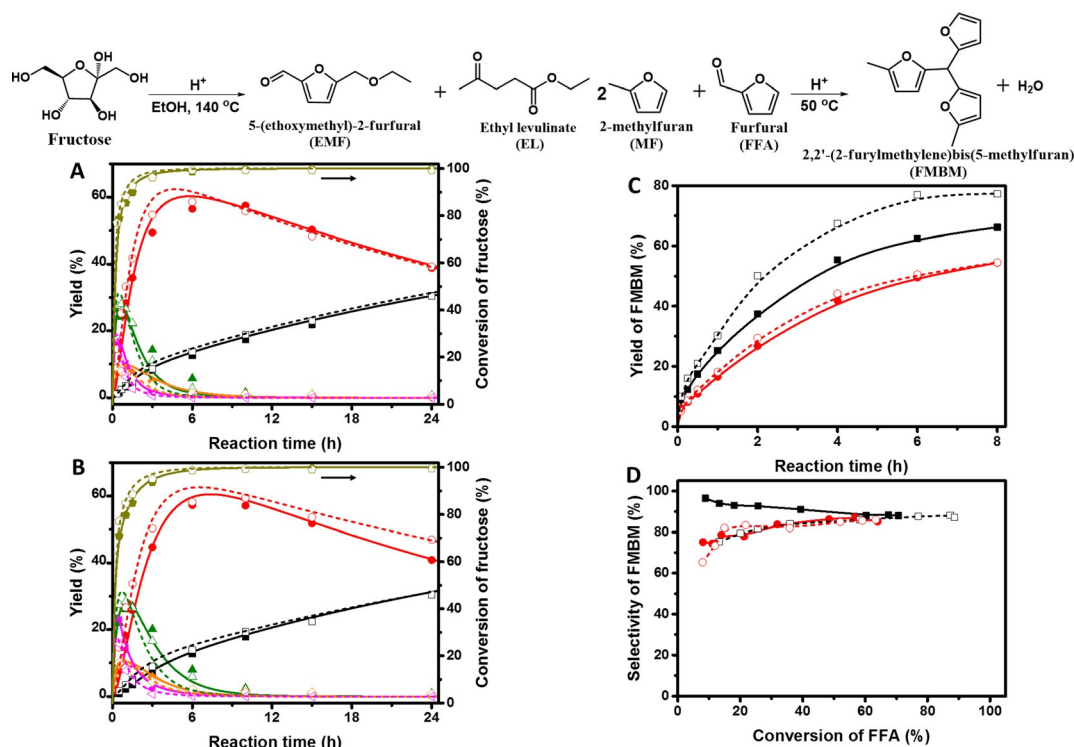
Figure 3. Kinetic profiles for the ethanolysis of fructose in the presence of a) $Si_{66}C_{33}Rot$-400-SO_3H (solid symbols and continuous lines) and $Si_{66}C_{33}TF$-400-SO_3H (open symbols and dashed lines) and b) $Si_{66}C_{33}Rot$-550-SO_3H (solid symbols and continuous lines) and $Si_{66}C_{33}TF$-550-SO_3H (open symbols and dashed lines). Reactant and products: fructose (●), EL (■), HMF ethers (●), HMF (▲), difructose anhydride (◄), glucosides (♦). Reaction conditions for the ethanolysis of fructose: fructose (180 mg), catalyst (50 mg), methyl naphthalene (20 mg) as internal standard, ethanol (2.67 g), 140 °C. c) Yield of FMBM versus reaction time and d) selectivity of FMBM versus conversion of FFA in the presence of $Si_{66}C_{33}Rot$-400-SO_3H (■), $Si_{66}C_{33}TF$-400-SO_3H (□), $Si_{66}C_{33}Rot$-550-SO_3H (●), and $Si_{66}C_{33}TF$-550-SO_3H (○). Reaction conditions for the condensation of sylvan: 2-methylfuran (13.2 mmol), furfural (6 mmol), catalyst (50 mg), naphthalene (20 mg) as internal standard, 50 °C.

(5-methylfuran) (FMBM), a C_{15} diesel precursor.[26–29] The production of this bulky and hydrophobic product requires the catalyst to be both porous and hydrophobic.[26] The $Si_{66}C_{33}Rot$-T-SO_3H catalysts possess large pore volumes (0.47 and 0.37 cm^{3}g^{-1} for $Si_{66}C_{33}Rot$-400-SO_3H and $Si_{66}C_{33}Rot$-550-SO_3H respectively) to ensure that the SO_3H groups easily contact the reactant molecules. Furthermore, the carbon sheets provide the desired hydrophobic surface to dispel generated H_2O and to shift the equilibrium (in the pores) towards the product. Therefore, as shown in Figure 3 c,d, the $Si_{66}C_{33}Rot$-T-SO_3H catalysts showed high selectivity towards FMBM ($>80\%$ at furfural conversions above 20%) over the entire reaction course with the continuous accumulation of FMBM. $Si_{66}C_{33}Rot$-400-SO_3H displayed higher activity than $Si_{66}C_{33}Rot$-550-SO_3H, mainly due to the higher density of SO_3H groups in the 400 °C-pyrolyzed sample. In the same way, $Si_{66}C_{33}TF$-400-SO_3H outperformed $Si_{66}C_{33}TF$-550-SO_3H. Overall, the rotary-synthesized composites were as active as the classic EISA ones for the reaction of sylvan.

In summary, a facile and robust method for the mass production of ordered mesoporous silica–carbon composites was proposed. After pyrolysis and sulfonation, great catalytic performances were demonstrated for two different chemical reactions, but other future (bulk) applications, such as the preparation of conductive materials, may also be considered

with these nanocomposites. The method, which is highly reproducible, comprises evaporation-induced self-assembly (EISA) under vacuum with rotation and may be promising to complement the standard thin film EISA approach towards the mass production of such powdery composites. The method can be easily extended to other one-pot, sol–gel organic-organic or organic–inorganic self-assembly syntheses to produce ordered mesoporous materials with versatile functional moieties.

Acknowledgements

[1] F. de Clippel, M. Dusselier, S. Van de Vyver, L. Peng, P. A. Jacobs, B. F. Sels, *Green Chem.* **2013**, *15*, 1398–1430.
[2] T. Ma, L. Liu, Z. Yuan, *Chem. Soc. Rev.* **2013**, *42*, 3977–4003.
[3] N. Pal, A. Bhaumik, *Adv. Colloid Interface Sci.* **2013**, *189–190*, 21–41.
[4] C. Liang, Z. Li, S. Dai, *Angew. Chem. Int. Ed.* **2008**, *47*, 3696–3717; *Angew. Chem.* **2008**, *120*, 3754–3776.

[5] A. Stein, S. G. Rudisill, N. D. Petkvoich, *Chem. Mater.* **2014**, *26*, 259–276.

[6] Y. Liang, L. Cai, L. Chen, X. Lin, R. Fu, M. Zhang, D. Wu, *Nanoscale* **2015**, *7*, 3971–3975.

[7] R. Zhong, L. Peng, F. de Clippel, C. Gommes, B. Goderis, X. Ke, G. Van Tendeloo, P. A. Jacobs, B. F. Sels, *ChemCatChem* **2015**, *7*, 3047–3058.

[8] Q. Hu, R. Kou, J. Pang, T. L. Ward, M. Cai, Z. Yang, Y. Lu, J. Tang, *Chem. Commun.* **2007**, 601–603.

[9] R. Liu, Y. Shi, Y. Wan, Y. Meng, F. Zhang, D. Gu, Z. Chen, B. Tu, D. Zhao, *J. Am. Chem. Soc.* **2006**, *128*, 11652–11662.

[10] C. J. Brinker, Y. Lu, A. Sellinger, H. Fan, *Adv. Mater.* **1999**, *11*, 579–585.

[11] D. Grosso, F. Cagnol, G. J. d. A. Soler-Illia, E. L. Crepaldi, H. Amenitsch, A. Brunet-Bruneau, A. Bourgeois, C. Sanchez, *Adv. Funct. Mater.* **2004**, *14*, 309–322.

[12] A. Gibaud, D. Grosso, B. Smarsly, A. Baptiste, J. F. Bardeau, F. Babonneau, D. A. Doshi, Z. Chen, C. J. Brinker, C. Sanchez, *J. Phys. Chem. B* **2003**, *107*, 6114–6118.

[13] H. Wei, Y. Lv, L. Han, B. Tu, D. Zhao, *Chem. Mater.* **2011**, *23*, 2353–2360.

[14] A. Sellinger, P. M. Weiss, A. Nguyen, Y. Lu, R. A. Assink, W. Gong, C. J. Brinker, *Nature* **1998**, *394*, 256–260.

[15] C. Matei Ghimbeu, L. Vidal, L. Delmotte, J. Le Meins, C. Vix-Guterl, *Green Chem.* **2014**, *16*, 3079–3088.

[16] L. Song, D. Feng, N. J. Fredin, K. G. Yager, R. L. Jones, Q. Wu, D. Zhao, B. D. Vogt, *ACS Nano* **2010**, *4*, 189–198.

[17] N. Yao, A. Y. Ku, N. Nakagawa, T. Lee, D. A. Saville, I. A. Aksay, *Chem. Mater.* **2000**, *12*, 1536–1548.

[18] T. Brezesinski, M. Groenewolt, A. Gibaud, N. Pinna, M. Antonietti, B. M. Smarsly, *Adv. Mater.* **2006**, *18*, 2260–2263.

[19] A. M. Cojocariu, X. Cattoen, R. Le Parc, D. Maurin, C. Blanc, P. Dieudonne, J.-L. Bantignies, M. W. C. Man, J. R. Bartlett, *Phys. Chem. Chem. Phys.* **2016**, *18*, 7946–7955.

[20] C. Xue, B. Tu, D. Zhao, *Adv. Funct. Mater.* **2008**, *18*, 3914–3921.

[21] S. Van de Vyver, L. Peng, J. Geboers, H. Schepers, F. de Clippel, C. J. Gommes, B. Goderis, P. A. Jacobs, B. F. Sels, *Green Chem.* **2010**, *12*, 1560–1563.

[22] W. Lou, Q. Guo, W. Chen, M. Zong, H. Wu, T. J. Smith, *ChemSusChem* **2012**, *5*, 1533–1541.

[23] R. Zhong, F. Yu, W. Schutyser, Y. Liao, F. de Clippel, P. A. Jacobs, G. Centi, L. Peng, B. F. Sels, *Appl. Catal. B.* submitted.

[24] T. Flannelly, S. Dooley, J. J. Leahy, *Energy Fuels* **2015**, *29*, 7554–7565.

[25] S. Saravanamurugan, A. Riisager, *Catal. Commun.* **2012**, *17*, 71–75.

[26] I. Ogino, Y. Suzuki, S. R. Mukai, *ACS Catal.* **2015**, *5*, 4951–4958.

[27] A. Corma, O. de la Torre, M. Renz, N. Villandier, *Angew. Chem. Int. Ed.* **2011**, *50*, 2375–2378; *Angew. Chem.* **2011**, *123*, 2423–2426.

[28] S. Li, N. Li, G. Li, L. Li, A. Wang, Y. Cong, X. Wang, T. Zhang, *Green Chem.* **2015**, *17*, 3644–3652.

[29] A. Corma, O. de la Torre, M. Renz, *Energy Environ. Sci.* **2012**, *5*, 6328–6344.